

0324

HIGH RESOLUTION STUDIES OF THE  
OF THE SOLAR ATMOSPHERE

Air Force Grant AFOSR-91-0244

Final Report

For the period 1 July 1991 through 31 July 1995

Principal Investigator

Shadia R. Habbal

February 1996

Prepared for

United States Air Force Office of Scientific Research

Bolling AFB, D.C. 20332-6448

DISTRIBUTION STATEMENT A

Approved for public release  
Distribution Unlimited

Smithsonian Institution  
Astrophysical Observatory  
Cambridge, Massachusetts 02138

The Smithsonian Astrophysical Observatory  
is a member of the  
Harvard-Smithsonian Center for Astrophysics

The USAF Program Manager for this Grant is Dr. Henry R. Radoski, U.S. Air Force  
Office of Scientific Research/NL, Building 410, Bolling AFB, D.C. 20332-6448

19960624 234

DTIC QUALITY INSPECTED 1

# HIGH RESOLUTION STUDIES OF THE STRUCTURE OF THE SOLAR ATMOSPHERE

## TABLE OF CONTENTS

1. Introduction .....	1
2. Summary of Results .....	1
2.1 Data Characteristics .....	1
2.1.1 <i>Space-based observations</i> .....	1
2.1.2 <i>Ground-based observations</i> .....	2
2.2 Data Analysis Tools .....	2
2.2.1 <i>Line ratio technique</i> .....	2
2.2.2 <i>Image difference technique</i> .....	3
2.2.3 <i>Image processing tools</i> .....	4
2.3 Results .....	6
2.3.1 <i>Temperature profile in coronal holes</i> .....	6
2.3.2 <i>Limits on the helium abundance in coronal holes</i> .....	8
2.3.3 <i>Morphology of the magnetic field structure in coronal holes</i> .....	10
2.3.4 <i>Morphology of the magnetic field structure in active regions</i> .....	12
2.3.5 <i>Characteristics of the temporal variability of the emission</i> .....	12
2.3.6 <i>Coronal mass ejections and radio noise storms</i> .....	14
3. Conclusion .....	20
4. References .....	21
5. List of Publications .....	22

## 1. INTRODUCTION

The coronal temperature, often exceeding one million degrees, is a direct manifestation of coronal heating processes. While this remarkable phenomenon remains to a great extent unaccounted for by the physical processes that we are currently aware of, it has fueled endless debates and countless research projects.

We have attempted to explore some aspects of this problem by pursuing two complementary directions: (1) the improved knowledge of the temperature structure of the solar corona, and (2) the study of the morphology of the magnetic field that defines it. Our approach has involved data acquisition of multiwavelength coordinated observations, image processing and data analysis.

This final report summarizes our main research projects and findings which have been accomplished with support from the Air Force for Scientific Research from July 1991 to September 1994. A list of publications resulting from these studies is given in Section 5.

## 2. SUMMARY OF RESULTS

Our approach has focused on exploring the physical characteristics of the coronal heating mechanisms, as manifested within different large scale magnetic structures, such as coronal holes, quiet regions and active regions. These explorations were made using different data sets, data analysis techniques and image processing tools. We present first the characteristics of the data used (section 2.1), we then describe the different analyses and image processing tools developed to study the plasma conditions, such as temperature, the characteristics of the variable emission, and the morphology of the open and closed structures in the solar corona (section 2.2). We highlight the results of these studies in section 2.3.

### 2.1 DATA CHARACTERISTICS

#### *2.1.1 Space-based Observations*

One of the outstanding characteristics of the EUV *Skylab* data obtained with the Harvard/SO55 Extreme Ultraviolet (EUV) spectroheliometer, was that the spectroheliograms were made simultaneously, through the same instrumental slit, in several wavelengths characteristic of chromospheric to coronal emission. To date, these characteristics have been unmatched by any subsequent mission. The field of view of the instrument was typically  $5' \times 5'$ , except during special observing sequences when smaller fields of view were scanned to allow for a higher temporal resolution (see Reeves et al. 1977 a,b). The field of view was rastered every 5.5 minutes with a spatial resolution of  $5'' \times 5''$ . Observations were made with different spectrometer grating settings. In the standard position, Mg X 625 Å ( $1.12 \times 10^6$ K), O VI 1032 Å ( $2.85 \times 10^5$ K), O IV 554 Å ( $1.5 \times 10^5$ K), C III 977 Å ( $7.4 \times 10^4$ K), C II 1336 Å ( $3.16 \times 10^4$ K), and Lyman  $\alpha$  1216 Å ( $2 \times 10^4$ K) were recorded. Alternative grating positions yielded, for example, Si XII 521 Å ( $1.8 \times 10^6$ K) and Ne VII 465 Å ( $5 \times 10^5$ K), together with other lines

sensitive to chromospheric emission. (The temperatures listed in parentheses correspond to the peak temperature of formation of the corresponding lines).

While our work has been based primarily on the EUV *Skylab* data, we have also explored selected observations from *Yohkoh*. The *Yohkoh* spacecraft was launched in 1991, and since, has returned x-ray observations of the Sun with an unprecedented temporal coverage (see Tsuneta et al 1991, Acton et al 1992). For our research we have been using the observations obtained with the soft x-ray grazing incidence telescope (SXT) onboard *Yohkoh* which forms whole sun images in the wavelength range 2-50 Å with a pixel size of approximately 5''. Images of selected regions of the Sun can also be obtained with a higher spatial resolution and temporal cadence.

### *2.1.2 Ground-based Observations*

Our ground-based observations consist primarily of data from the National Solar Observatory at Sacramento Peak (NSO/SP), and the Very Large Array (VLA). Observations of the Fe X 6374 Å and Fe XIV 5303 Å lines were made with the Fisher-Smartt Emission Line Coronal Photometer (ELCP) (Smartt, 1982). This instrument photoelectrically records the solar corona when fed with the Evans Solar Facility 40 cm Coronagraph. Scans are recorded around the solar limb with a 1.1' aperture, in angular steps of 3° in latitude. The coronagraph allows observations to start at a heliocentric distance of  $1.1 R_s$  and extend reliably out to 1.2-1.3  $R_s$ . Photographic images of the corona in H  $\alpha$ , Fe X and Fe XIV were also obtained with the one shot coronagraph. Image processing techniques were applied to the subsequently digitized images.

Observations were also obtained at several cm wavelengths with the radio telescopes at the Very Large Array (VLA), in coordination with other ground- (e.g. NSO/SP) and space-based observations (e.g. SPARTAN, *Yohkoh*, and NIXT). With this instrument, the field of view depends on the wavelength used, and the spatial resolution depends on both wavelength and configuration of the radio antennas. Our observations were made typically at 6, 20 and 90 cm.

## 2.2 DATA ANALYSIS TOOLS

### *2.2.1 Line Ratio Technique*

The inference of the coronal temperature from the ratio of the intensities of emission lines depends on the assumption that the density and temperature are constant along a given line of sight from which the emission from different spectral lines is observed. In the absence of direct measurements of the coronal temperature, the line ratio technique is the most commonly used. To apply this technique, one compares the ratios of line intensities deduced from observations with those derived theoretically. The intensity of an emission line at a

given wavelength  $\lambda$  can be written as

$$I_\lambda = \int_L P_\lambda N_e N_H ds, \quad (1)$$

in  $\text{ergs cm}^{-2} \text{s}^{-1} \text{str}^{-1}$ , where the emissivity,  $P_\lambda$ , is given by (see, e.g. Raymond 1988, and references therein)

$$P_\lambda = 8.63 \cdot 10^{-6} A_{\text{el}} \frac{N_{Z,i}}{N_Z} \frac{\Omega}{\omega \sqrt{T}} e^{-E/kT} h\nu. \quad (2)$$

In these expressions, the integral is along the line of sight,  $L$ .  $N_e$  and  $N_H$  are the electron and hydrogen(proton) densities respectively. The elemental abundance  $A_{\text{el}}$  is given with respect to hydrogen,  $\frac{N_{Z,i}}{N_Z}$  is the ionization fraction,  $\Omega$  is the collision strength,  $\omega$  is the degeneracy of the ground state, and  $E$  is the threshold energy usually taken to be equal to the photon energy  $h\nu$ . It is clear from this expression that the ratio of the emissivity (or equivalently, intensity) of two lines from different elements then reduces to a functional dependence on temperature, as well as on the ratio of the abundances of the ions involved. Since the elemental abundances are poorly known, no unique temperature can be determined from only one line ratio. However, with the availability of three or more lines, and hence three or more ratios, one can restrict the temperature range thus inferred (see Habbal, Esser and Arndt 1993). The uncertainties are significantly alleviated when different lines from the same element can be measured.

### 2.2.2 Image Difference Technique

To characterize the properties of the intermittent component of the coronal heating processes, independently of the magnetic structures studied, i.e. whether in coronal holes, quiet or active regions, we expanded on a method developed by Habbal and Grace (1991). The approach is as follows: the change in the intensity in any of the pixels making up a given image raster is considered significantly variable if the absolute value of the difference in intensity in a given pixel, at two consecutive times, is greater than  $2\sigma$ , i.e. if

$$\delta I = |I_{t_1} - I_{t_2}| > 2\sigma \quad (3)$$

where  $\sigma = \sqrt{\bar{I}}$ ,  $\bar{I} = \frac{I_{t_1} + I_{t_2}}{2}$  is the average of the intensities  $I_{t_1}$  and  $I_{t_2}$  within each pixel of the images, measured at times  $t_1$  and  $t_2$ .  $\frac{\delta I}{\bar{I}}$  then represents the relative change of the intensity between two consecutive time frames for which the variability is significant. We also introduce the measure,  $\frac{\delta n}{N}$ , or spatial density of variability, defined as the ratio of the number of variable pixels satisfying condition (1) to the total number of pixels  $N$  in a given area. Although we applied this technique primarily to EUV/*Skylab* spectroheliograms, it is readily applicable to different data sets, as long as the difference in time between two consecutive scans is such that the drift due to solar rotation within this time interval is much smaller than the pixel size in the scans.

### 2.2.3 Image Processing Tools

We describe here two different image processing tools that we have found to be powerful in improving the spatial resolution and enhancing the fine scale structures in the images. These are the Blind Iterative Deconvolution Algorithm (BID), and the Image Enhancement Algorithm (IEA).

BID is a technique that allows one to recover simultaneously, from an image with degraded resolution, the point spread function (PSF) and the high angular resolution image through an iterative process. It was originally developed for the correction of the effects of atmospheric turbulence in optical images (Ayers and Dainty 1988) and was modified for astronomical and solar images (Nisenson et al 1989, Karovska and Habbal 1991). When applied to high signal-to-noise images, degraded by an unknown linear and stationary function, this algorithm finds a pair of functions corresponding to the degrading function and the undegraded image, which when convolved reproduce the input image within given physical constraints. The first step in the iterative process is to deconvolve the degraded image with an estimate of the PSF using signal-to-noise ratio constraints. The result of the deconvolution is transformed back to the image space, and several physical constraints, including positivity and limited domain of the image, are applied. Once the new estimate of the PSF is obtained, it is used to deconvolve the input image in the next iteration. The iteration continues until some concluding criterion is reached, such as image quality criterion or a limit on the number of cycles. Examples of recovered PSF's for space observations from *Skylab* and *Yohkoh* are shown in Figure 1b and 1c. In both examples, the starting guess for the PSF was a Gaussian with random noise and half power width radius of 5 pixels (Figure 1a). Substantial sharpening of the structures in the images occurred after 200 iterations, as seen in the example of the *Yohkoh* image in Figure 1d and 1e, and the iterative process was stopped when the reconstructed image remained effectively unchanged in further cycles of the BID. The elongation in the reconstructed PSF from the *Yohkoh* data, is probably due to the off-axis response of the telescope mirror. We note that there is evidence of ellipticity in the instrumental PSF in the measurements made before the flight (see Maartens et al 1994).

To explore the structure of the solar atmosphere at the limb, from the chromosphere to the lower corona, we developed a version of the image enhancement algorithm (IEA) originally proposed by Koutchmy et al (1988) (Karovska, Blundell and Habbal 1994). This algorithm detects the location of a significant change in grey level in the image; thus, it enables us to obtain information regarding the spatial characteristics of the small scale structures despite the presence of noise and the high dynamic range between the small and large scale structures. This algorithm calculates the maxima of the multidirectional second derivatives of the intensities in a given image using the following nonlinear operator (see Koutchmy et al 1988):

$$M(I) = \alpha M8(I) + \beta E2(M8(S2(I))) + \gamma E4(M8(S2(S2(I)))) + \dots \quad (4)$$

The operator M8 calculates the maximum of the second derivatives in eight directions, S2 is an averaging operator, E2 and E4 expand the image with factors of two and four, respectively,

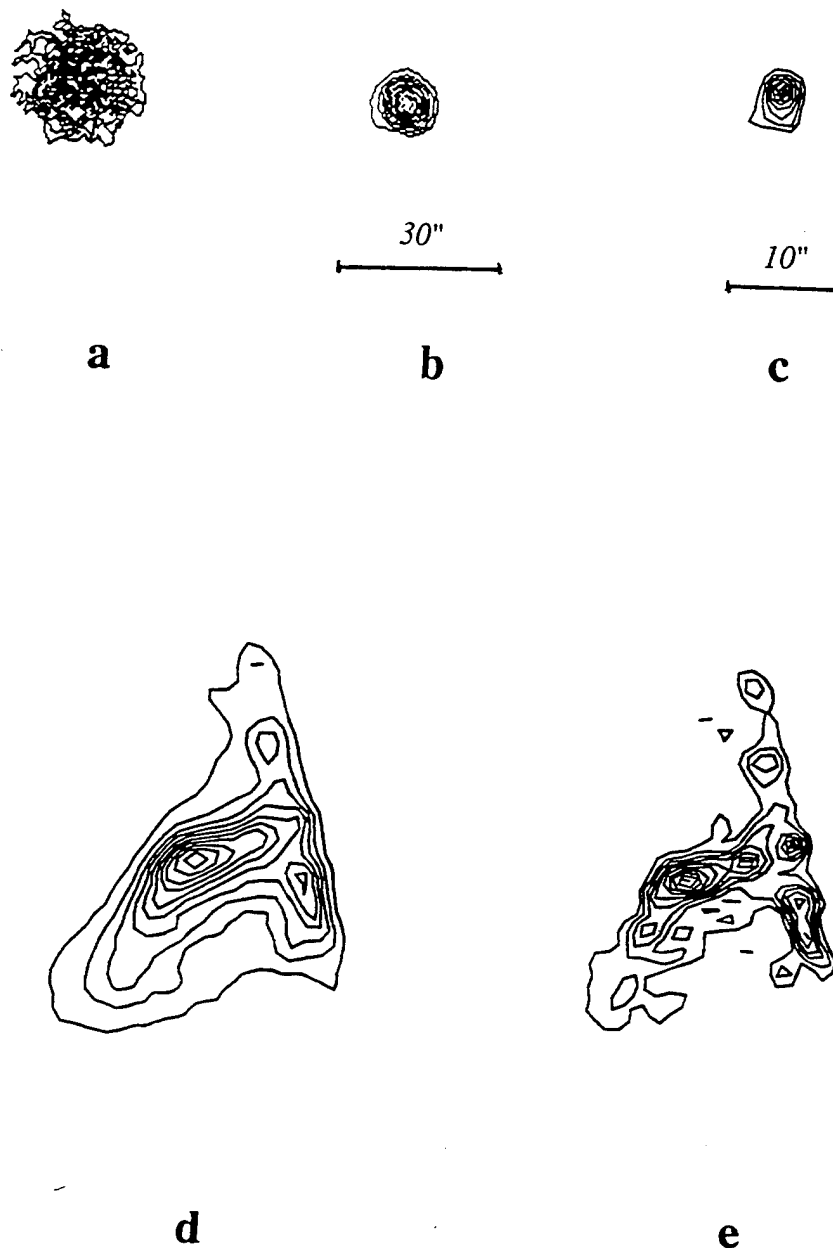


Figure 1: (a) Starting PSF (random Gaussian), (b) reconstructed PSF for a C III *Skylab* image, (c) reconstructed PSF for *Yohkoh* image in (d), (d) *Yohkoh* image taken on 17 April 1993 of a compact bright source at the solar limb, and (e) reconstructed *Yohkoh* image. The lowest contour levels are at 10% of the maximum, i.e. at the noise level.

and  $I(i,j)$  is the intensity in a given pixel (i,j). Several levels of block-average smoothing may be applied prior to computing the derivative, depending on the signal-to-noise ratio in the image, and the characteristic scale of the structures in the image that one would like to enhance. The coefficients  $\alpha$ ,  $\beta$ , and  $\gamma$  are weights chosen to select different levels of block-average smoothing.

## 2.3 RESULTS

### 2.3.1 Temperature profile in coronal holes

Coronal holes are believed to be the source region of fast solar wind streams (see, for example, reviews in Zirker 1977). The temperature profile in the inner corona is one of the indicators of the coronal heating process within these regions. It also plays an important role in determining the flow properties of the solar wind at 1 AU (e.g., Parker 1958, Leer and Holzer 1991). No single instrument to date has measured directly the temperature profile over a heliocentric distance exceeding a fraction of a solar radius. Estimates of this profile are derived from a combination of inferences, such as shown in Figure 2.

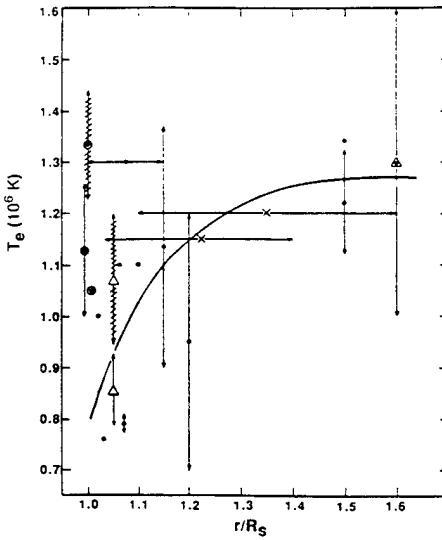


Figure 2: Temperature gradient in the inner corona as derived from limb (filled circles, and open triangles), disk (open circles with filled centers) and in situ observations (triangle with filled circle). Arrows indicate the ranges derived from observations. Hatched arrows represent measurements clearly made at and/or outside boundaries of coronal holes. (From Habbal, Esser and Arndt 1993).

Using Mg X, Ne VII and O VI line intensities, measured with the EUV/*Skylab* experiment, off the solar limb in a polar coronal hole, Habbal, Esser and Arndt (1993) applied the line ratio technique to derive the temperature below  $1.1 R_s$ . Although formed at much cooler temperatures, the O VI line can be used since it has a very broad response function to temperatures reaching  $10^6$  K. The temperature across the coronal hole thus inferred is shown

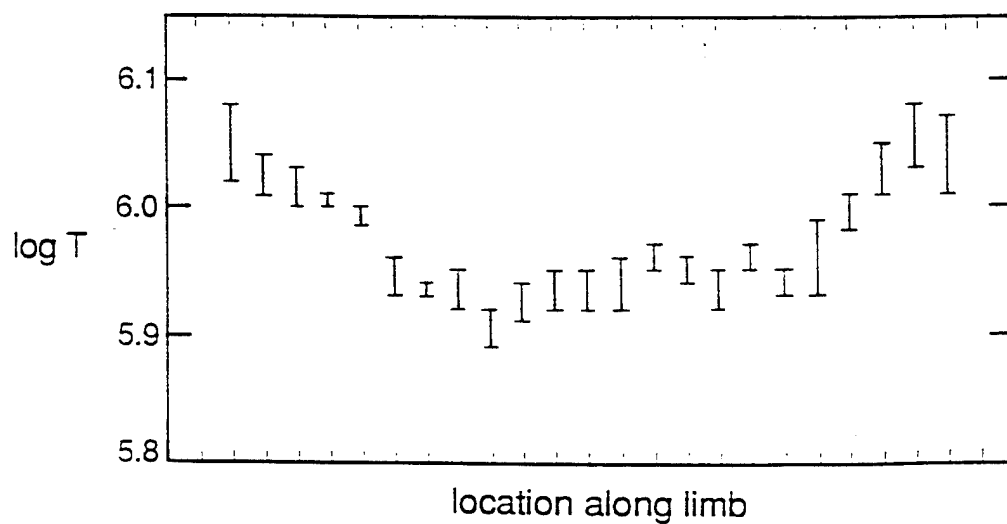
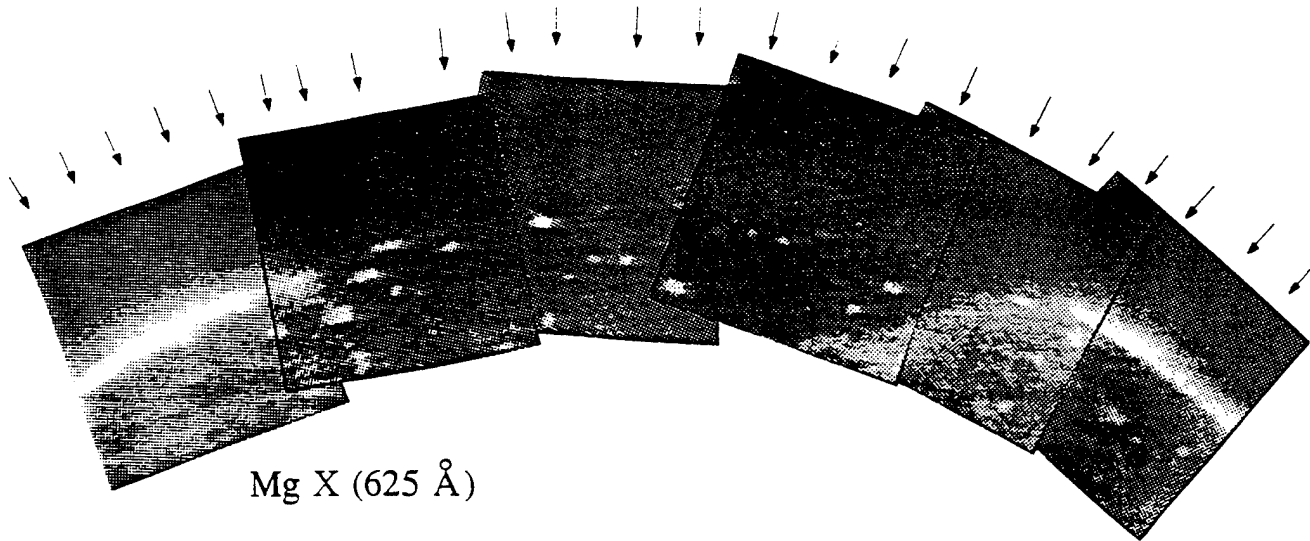


Figure 3: Temperature distribution across a south polar coronal hole and neighboring quiet regions as inferred from ratios of line intensities of Mg X, Ne VII and O VI. The upper panel shows the composite image in Mg X, where the coronal hole is distinguished by the very low emission with the exception of bright points. The arrows indicate the radial directions along which temperatures were inferred. (From Habbal, Esser and Arndt 1993).

in Figure 3. The top panel shows the composite made from a sequence of Mg X images spanning a south polar coronal hole and its boundaries. The arrows indicate the radial directions along which the line intensities were measured, and the temperature subsequently inferred. Since the intensity of the lines decreases very rapidly with heliocentric distance, the data are reliable only out to  $1.07 R_s$ . The error bars take into account the uncertainties entering such an inference, as well as the average temperature range within the field of view, along a given radial direction.

A similar study was carried out with more recent ground-based measurements of the Fe X 6374 Å and Fe XIV 5303 Å line intensities made at NSO/SP. These lines have a peak temperature of formation of  $10^6$  K and  $1.8 \times 10^6$  K respectively. Although data were taken for all latitudes,  $\phi$ , we present here the results for the south polar coronal hole (Figure 4). The boundaries of the coronal hole are very sharply defined by the gradient of the Fe XIV intensity and were found to match very closely those determined from the *Yohkoh* soft x-ray observations. Although made at different heliocentric distances, and different times, the trend of the temperature profile across the coronal hole is very similar to that derived from the EUV data and shown in Figure 3. It is clear, however, that the use of this combination of iron lines fails in coronal holes when the Fe XIV emission is absent (see, for example, the intensity of Fe XIV for  $150^\circ < \phi < 162^\circ$ , at  $1.1 R_s$ , Figure 4). When present, a significant fraction of the Fe XIV emission is contributed by the hot material veiling the coronal hole and lying along the line of sight. Hence, the temperature inferred from these two lines should be regarded as an upper limit to the coronal hole temperature.

These two examples show that temperature inferences depend on the choice of spectral lines used, and that there is a marked difference between the temperature inferred in coronal holes and its boundaries. The larger temperature inferred for the boundaries of coronal holes is a good indicator of the potential effect of the line of sight contamination if we envision that such material could also be lying along our line of sight, except in rare cases when the extent of the coronal hole along the line of sight is very large. This extent can in fact be determined from full disk soft x-ray observations, such as from *Yohkoh*.

### *2.3.2 Limits on the helium abundance in coronal holes*

Another important parameter for understanding the properties of the solar wind flow is the helium abundance in the inner corona,  $\alpha$ , defined as the ratio of helium to proton number densities. A number of theoretical studies have shown that the helium abundance in the inner corona could be significant, i.e.  $>> 0.1\text{--}0.2$ , and that fully ionized helium, or  $\alpha$  particles, could play an important role in the flow properties of electrons and protons in the solar wind (see, e.g. Geiss et al 1970, Bürgi and Geiss 1986, Bürgi 1992, Leer, Holzer and Shoub 1992). Observationally, the helium abundance is very hard to determine due to the difficulty of measuring helium lines in the corona (see discussion in Leer, Holzer and Shoub 1992). Recently, we presented a simple technique for inferring limits on the helium abundance in the inner corona from knowledge of the density, temperature and their respective gradients in that region (Habbal and Esser 1994). We also showed that in the absence of density

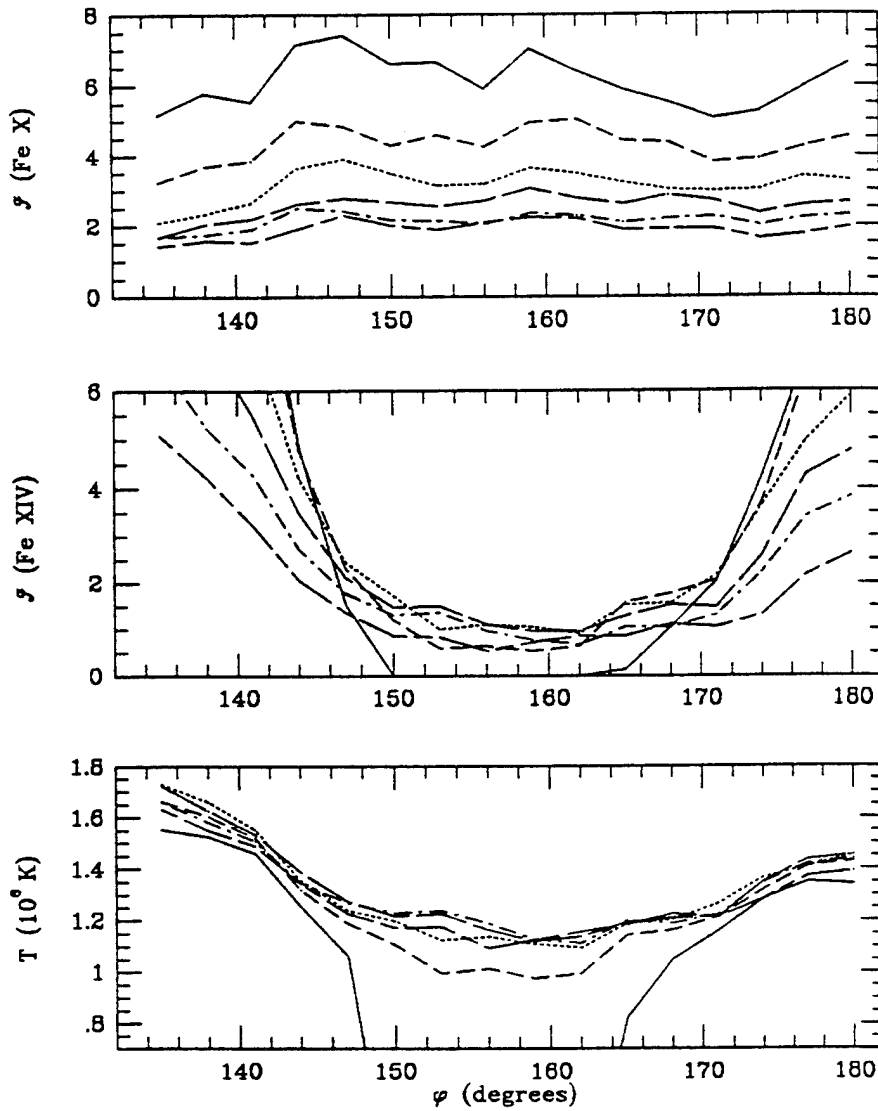


Figure 4: Plot of Fe X 6374 Å intensity, Fe XIV 5303 Å intensity, and line ratio temperature,  $T$ , as inferred from these two lines, versus latitude  $\phi$ , for a south polar coronal hole observed on 10 April 1993. Measurements are shown at heliocentric distances of 1.1 (solid line), 1.12 (short dashes), 1.14 (dotted line), 1.16 (long dashes), 1.18 (dash-dotted line), and 1.20  $R_s$  (long-short dashes).

measurements, these can be substituted by line intensity measurements and their gradients in the inner corona. Using the same EUV/*Skylab* data as shown in Figure 3, we inferred a *lower* limit to  $\alpha$  of 0.3 at the base of coronal holes. For radial distances at which the temperature reaches a maximum and then starts to decrease, an *upper* limit to  $\alpha$  can be derived. The example used was for a coronal hole but is readily applicable to different coronal structures. Thus, by applying this technique, inferences of limits on the helium abundance in the inner corona can be made with data readily available and to be acquired in the future either with space- and/or ground-based observations.

### 2.3.3 Morphology of the magnetic field structure in coronal holes

Knowledge of the plasma parameters characteristic of coronal holes is but one aspect of the exploration of the coronal heating mechanism(s). Another aspect, often overlooked, is the fine scale morphology of the magnetic field itself. Macrospicules and polar plumes are the dominant structures in coronal holes. As seen in EUV/*Skylab* observations made simultaneously at different wavelengths off the limb, these structures are prominent at different temperatures and have different lifetimes (see, e.g. Habbal 1992). Macrospicules are most prominent in lines formed between  $10^4$  K and  $10^5$  K. They appear as columns of chromospheric material, reminiscent of giant spicules, extending anywhere from 10 to 60" above the solar limb. Their characteristic lifetime ranges from 3 to 45 min (Dere et al 1989). Extreme ultraviolet (EUV) and radio observations suggest that they have cool  $10^4$  K plasma cores, with a thin outer sheath not exceeding  $3 \times 10^5$  K (Withbroe et al 1976, Habbal and Gonzalez 1991). The macrospicules shown in Figure 5, which are the largest EUV macrospicules observed to date, have a spatial frequency of occurrence of approximately 1.5', very similar to that of polar plumes also present in these limb observations (see Karovska, Blundell and Habbal 1994). While visible only in lines formed above  $10^6$  K, polar plumes define the extended structure of coronal holes as seen in eclipse photographs (e.g. Koutchmy 1977). Recent work by Thieme et al (1989) suggests that remnants of polar plumes are observed in interplanetary space.

Application of the image enhancement algorithm, IEA, to EUV limb observations of a north polar coronal hole made with *Skylab*, exposed the spicules at the limb (Figure 5, bottom panel.) The substructure of the spicules and macrospicules as exposed by the application of IEA is shown in Figure 5. While the limb appears as a jagged boundary in the original image, the processed image revealed, for the first time in the EUV, a forest of spicule-like structures, with a characteristic spatial separation of 10" to 15" (Karovska, Blundell and Habbal 1994). It also revealed the existence of substructures within macrospicules and plumes. The processed images showed that macrospicules consist of column like structures, with a diameter of about 5" - the resolution limit of the telescope, often with a hook-like shaped tip. The processing also exposed low lying arches (about 5"-10" in height) which were commonly found to be associated with their bases. The enhanced images of polar plumes, as observed in O VI and Mg X, revealed the presence of filamentary substructures which extended to at least 4', the edge of the field of view, with the same characteristic spatial separation of 10"-15". The enhanced images also showed that spicules, and the substructures

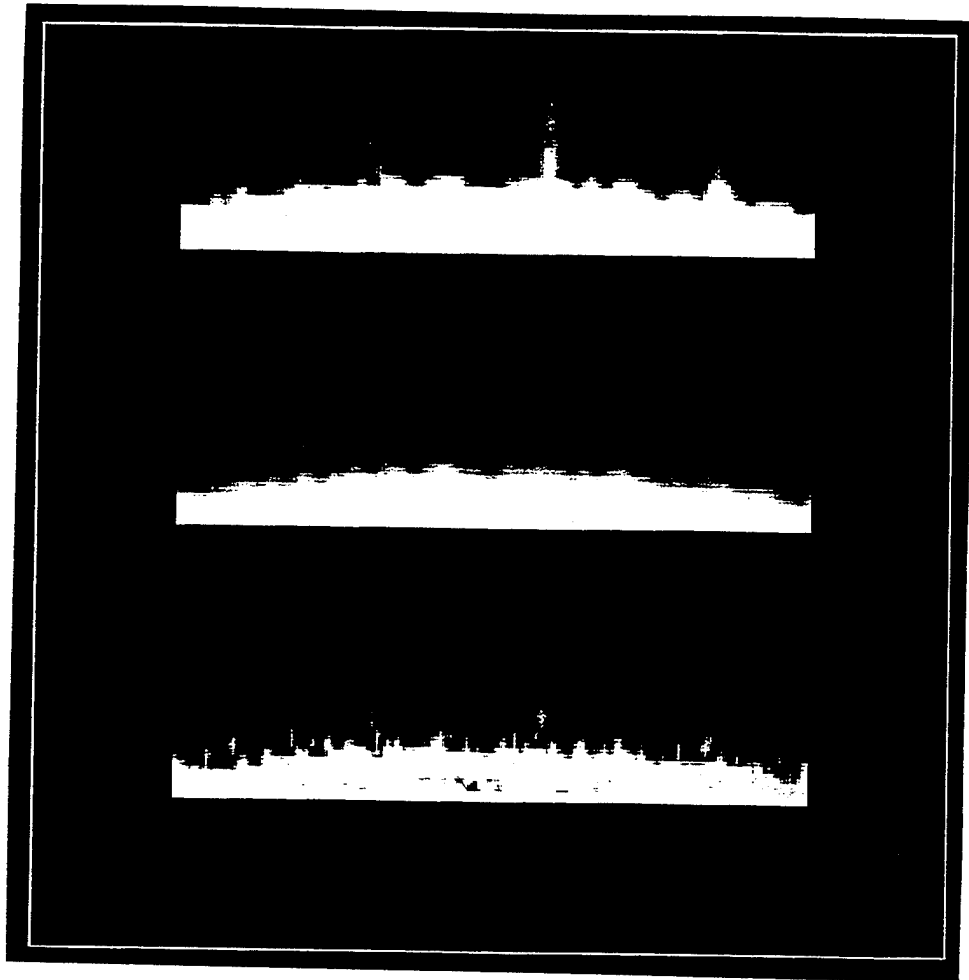


Figure 5: Structures observed at the solar limb in C III 977 Å in a south polar region. Unprocessed image with contrast that emphasizes macrospicules (top panel), unprocessed image with contrast that emphasizes the region at the limb (middle panel), and image processed with IEA (bottom panel). (From Karovska, Blundell and Habbal 1994).

within macrospicules and polar plumes, observed at different temperatures, are not cospatial.

#### *2.3.4 Morphology of the magnetic field structure in active regions*

The discrete nature of the coronal emission is also a common characteristic of closed magnetic structures such as bright points, active and quiet regions (quiet regions are defined as regions of diffuse emission in large scale closed magnetic structures). Application of IEA to simultaneous multiwavelength *Skylab* observations showed that the diffuse emission in active regions is resolved into distinct loops (Arndt, Habbal and Karovska 1994). This technique also confirmed that distinct loops at different temperatures, such as Si XII and Ne VII shown in Figure 6, are not cospatial but coexist within the same active region complex, a characteristic also found in the miniature loops forming coronal bright points (e.g., Habbal and Grace 1991). The image enhancement also showed that the basic spatial scale in their substructures is the same in different temperature loops, a finding which is not obvious in the unprocessed images. Similar results, i.e. the lack of cospatiality and discrete nature of the loops, were found when IEA was applied to ground-based observations of Fe X and Fe XIV of a quiet sun region observed off the limb (Figure 7).

#### *2.3.5 Characteristics of the temporal variability of the emission*

The application of IEA to a time sequence of the macrospicule observations shown in Figure 5, showed the continuous interaction between their 5"-10" substructures, with the occasional ejection of plasma following a ballistic trajectory (see Karovska and Habbal 1994). The processed images also revealed evidence of some pinching off, probably leading to the ejection of plasma (see, e.g. Figure 8 at 23:07:36 UT), as had been reported by Habbal and Gonzalez (1991) in radio observations at 4.8 GHz. The processed images showed for the first time that the base of macrospicules is formed of arches from which the twisted substructures that form the macrospicules originate (as seen by comparing frames 22:56:07 and 22:59:14 UT in Figure 8). The morphology of the substructures within the macrospicules changes as well. In fact, some of the most dramatic changes occur at the base of the macrospicules where the small arch-like structures reorganize their morphology within one minute, the shortest temporal resolution available in these data.

Applying the image difference technique and image processing tools, to an active region complex, we found that the variable emission from this complex is distinctly localized around the footpoints, as seen by the white contours in Figure 6 (see Arndt, Habbal and Karovska 1994). In coronal holes and quiet regions, this variability is found to be localized at the intersection of network cells, and in bright points (see Habbal and Grace 1991). The spatial density of the variability,  $\delta n/N$  (as defined in section 2.2.2), has a very characteristic temperature dependence with a peak at  $10^5$ K, in either coronal holes, quiet or active regions, as shown in Figure 9 (Habbal, Arndt, and Karovska 1994). We also point out that the vertical bars, which show the extent of this measure as a function of time, do not extend by more than 15%. Another striking characteristic is that the difference in the magnitude of  $\delta n/N$ ,

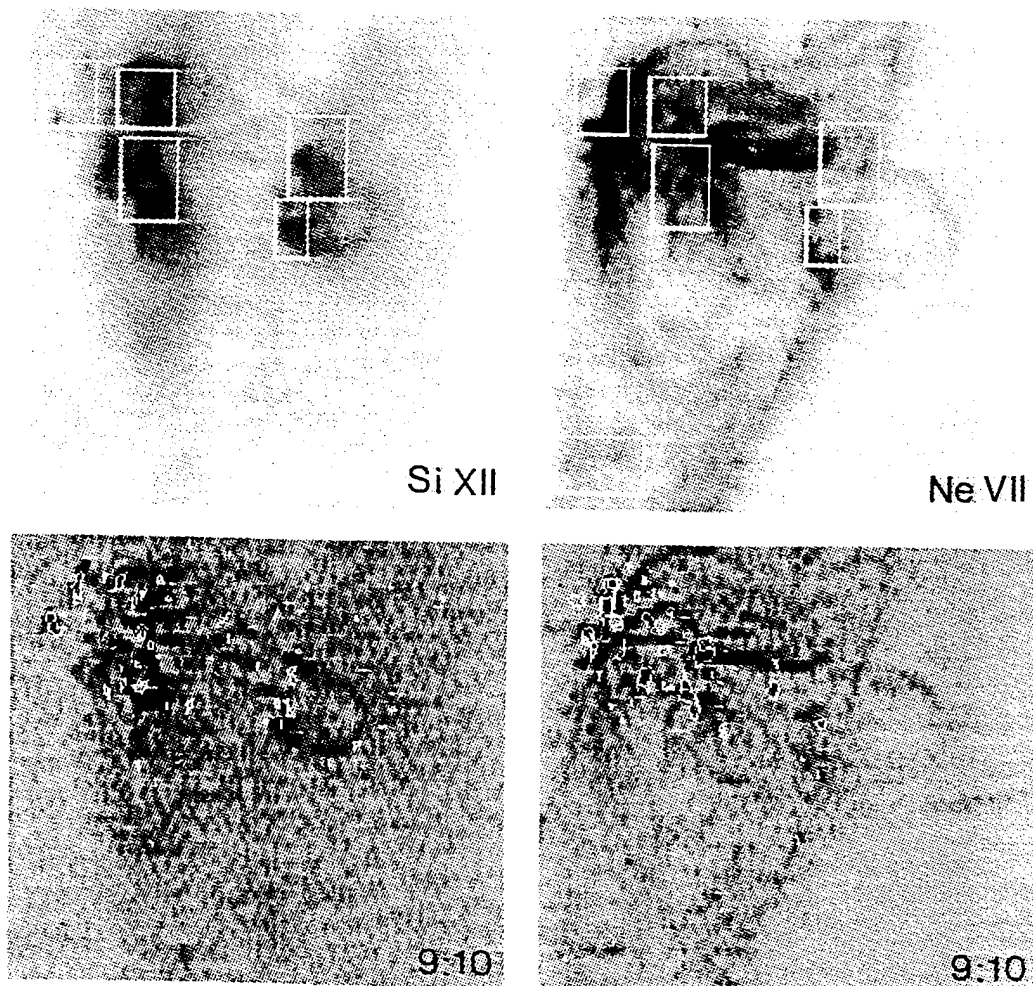


Figure 6: Unprocessed (top panels) and IEA processed images (bottom panels) of an active region complex observed simultaneously in Ne VII and Si XII. The white contours in the lower panels indicate the location of the significant variability, as determined by condition (3). (From Arndt, Habbal and Karovska 1994.)

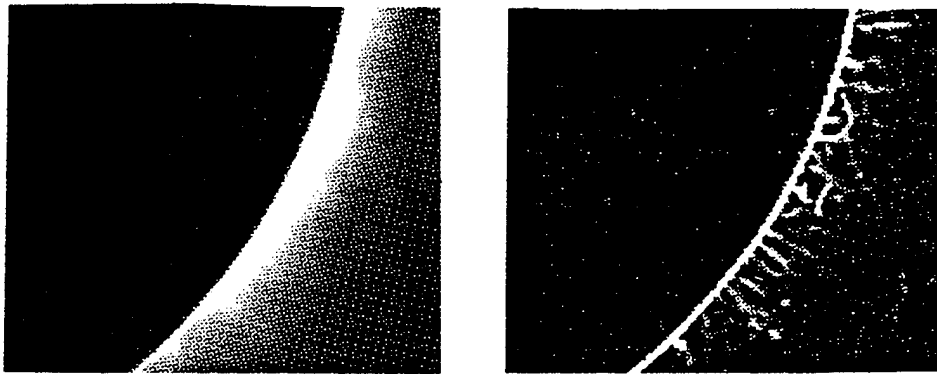


Figure 7: Unprocessed (left panel) and processed (right panel) images of a quiet region observed in Fe XIV 5303 Å at NSO/SP.

between all three regions does no exceed 10%. In active regions, the magnitude of  $\delta n/N$  seems to be independent of any flaring activity, as shown in Figure 10a. A flare is evident only in the relative magnitude change of the intensity (Figure 10b). These results point to common characteristic properties of the underlying small scale magnetic field which are independent of the overlying large scale magnetic structures, whether they are open field lines such as in coronal holes, or closed field lines such as in active or quiet regions.

### 2.3.6 Coronal mass ejections and radio noise storms

Acquisition and analysis of both disk and limb observations were made to examine the changing conditions of the low solar corona, below  $1.5 R_s$ , preceding and following a coronal mass ejection observed on the west limb on 12 April 1993. The disk observations comprised 90 cm (333 MHz) radio and daily *Yohkoh* soft X-ray measurements, while the limb observations included measurements of emission from X-rays, Fe X 637.4 nm and Fe XIV 530.3 nm coronal lines, and Thomson scattered white-light. The analysis of the disk and limb observations showed that throughout the three days of consecutive observations, the occurrence and persistence of nonthermal emission at 90 cm — also known as type I noise storm emission — was associated with the large-scale coronal magnetic structures where the coronal mass ejection eventually occurred (see Figure 11). However, off-limb observations of the corona gave no indication of changes, either preceding or following the event, other than a subsequent flare observed in X-rays, that were markedly different from changes in other neighboring structures (Figures 12 and 13). The analysis of this novel combination of data supports the current view that coronal mass ejections are independent of the “classical” solar activity in the low corona. The radio observations, on the other hand, are a strong advocate for the connection between noise storms and coronal mass ejections, without implying, however,

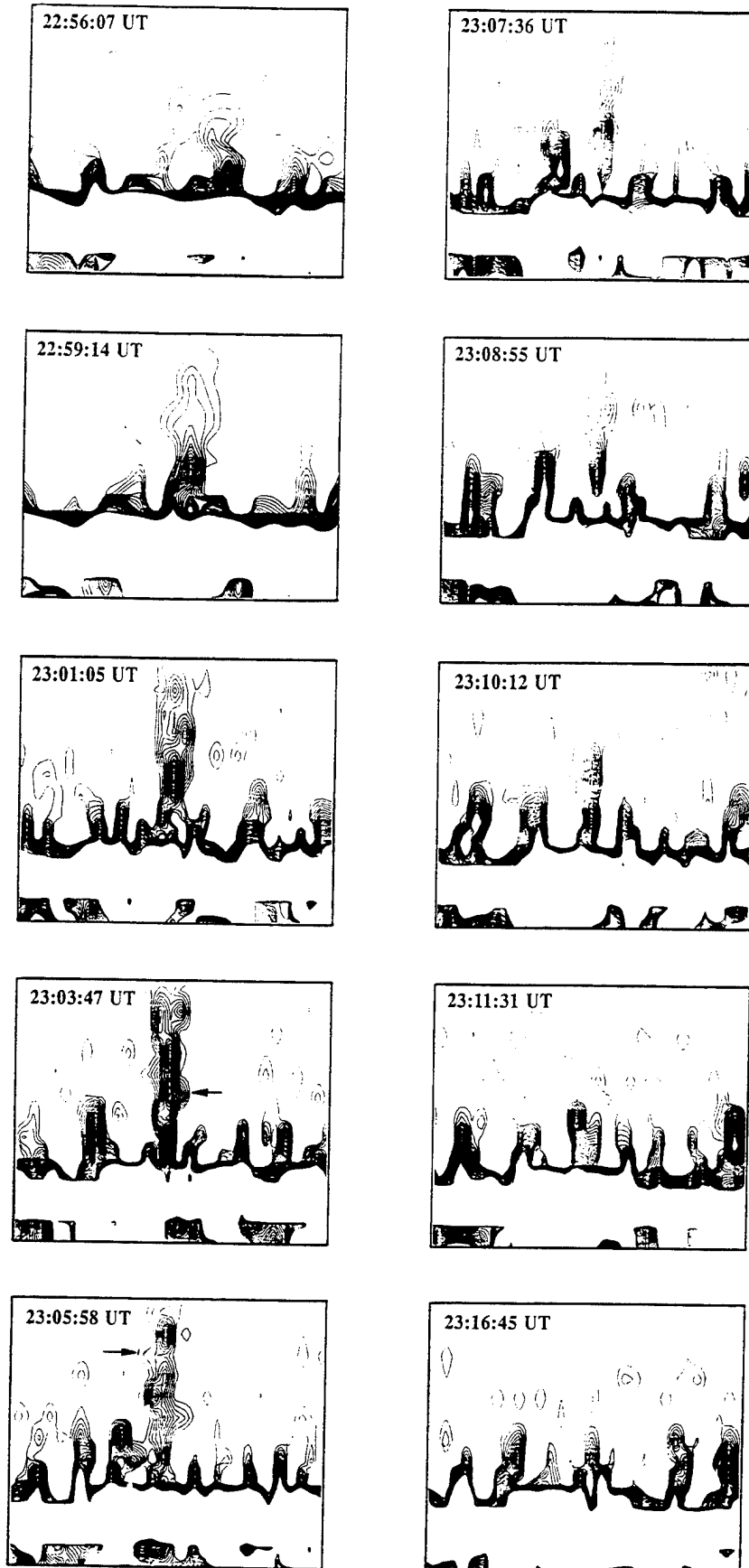


Figure 8: A time sequence of a section of Figure 5, showing the evolution of the central macrospicule as evidenced in the processed images. The width of each panel is 75". (From Karovska and Habbal 1994).

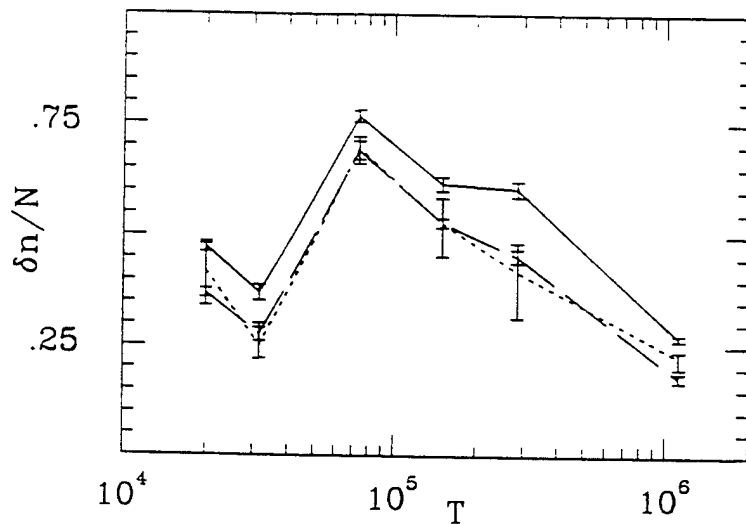


Figure 9:  $\frac{\delta n}{N}$  versus temperature for an active region (solid line), a quiet region (dashed line) and a coronal hole (dotted line). (From Habbal, Arndt and Karovska 1994).

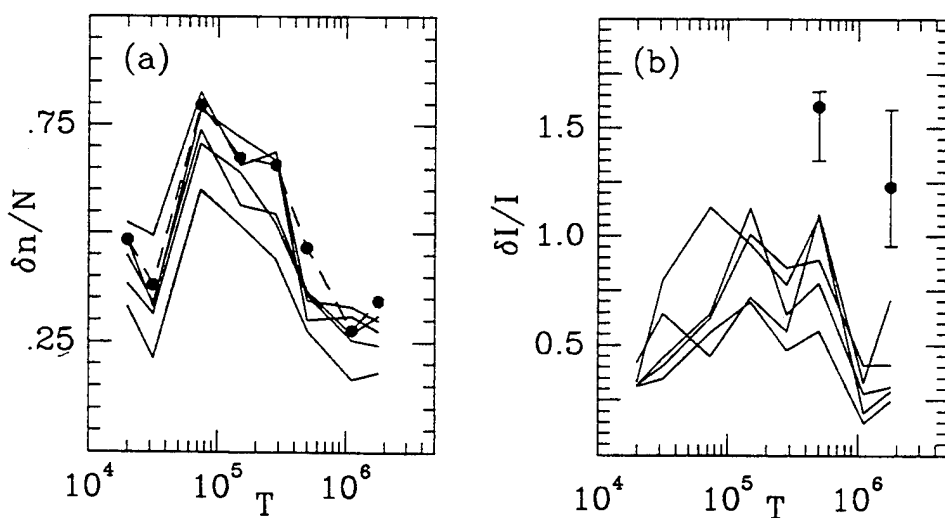


Figure 10: a)  $\frac{\delta n}{N}$  versus temperature for the regions defined by the boxes in Figure 5. The dashed curve is for the flaring region. (b)  $\frac{\delta I}{I}$  versus temperature for the same sections of the active region as (a). The values of  $\frac{\delta I}{I}$  for the flare are given only for Ne VII and Si XII, the wavelengths at which it was recorded, with the vertical bars indicating the spread of this measure as a function of time. (From Habbal, Arndt and Karovska 1994).

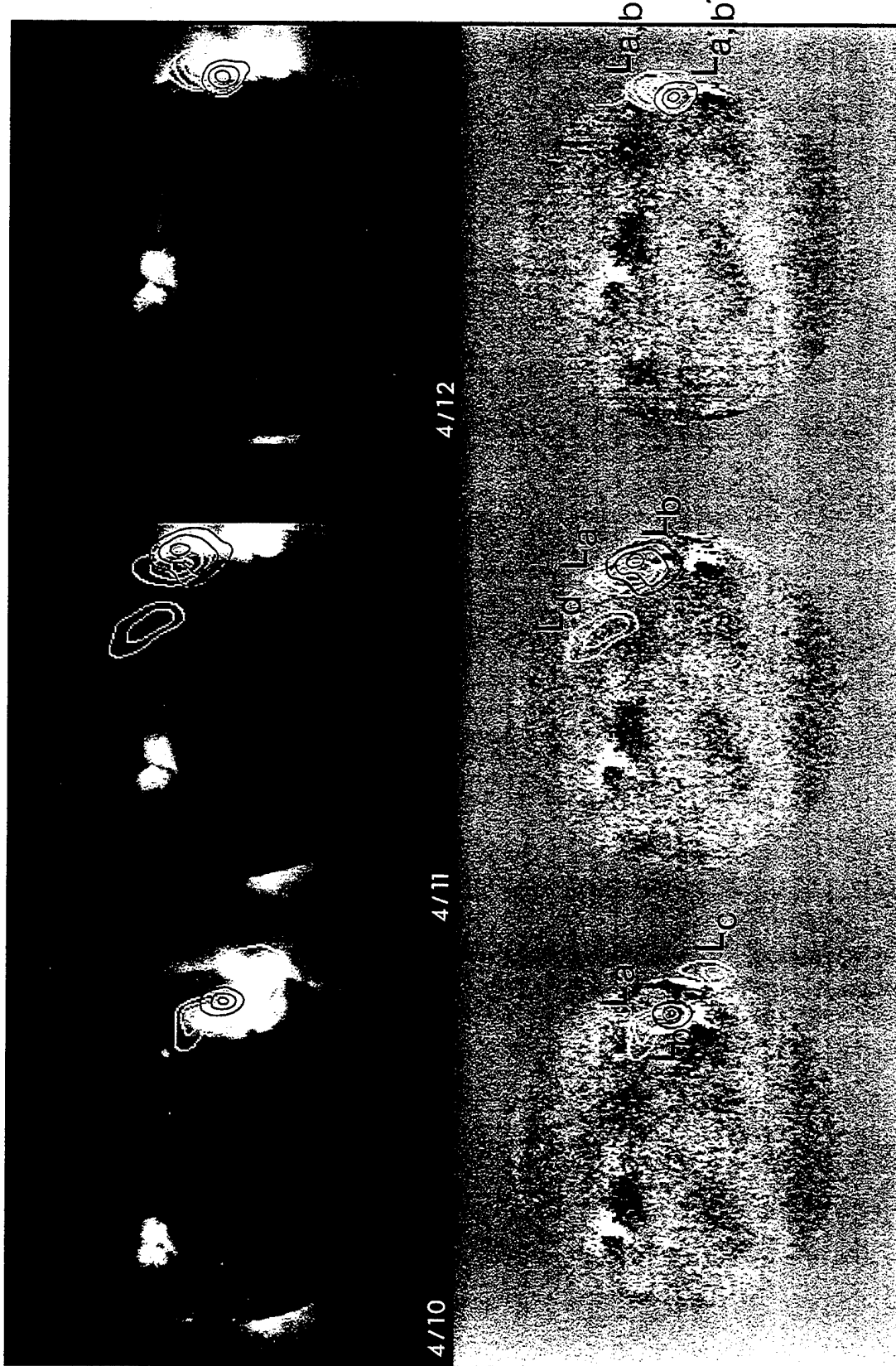
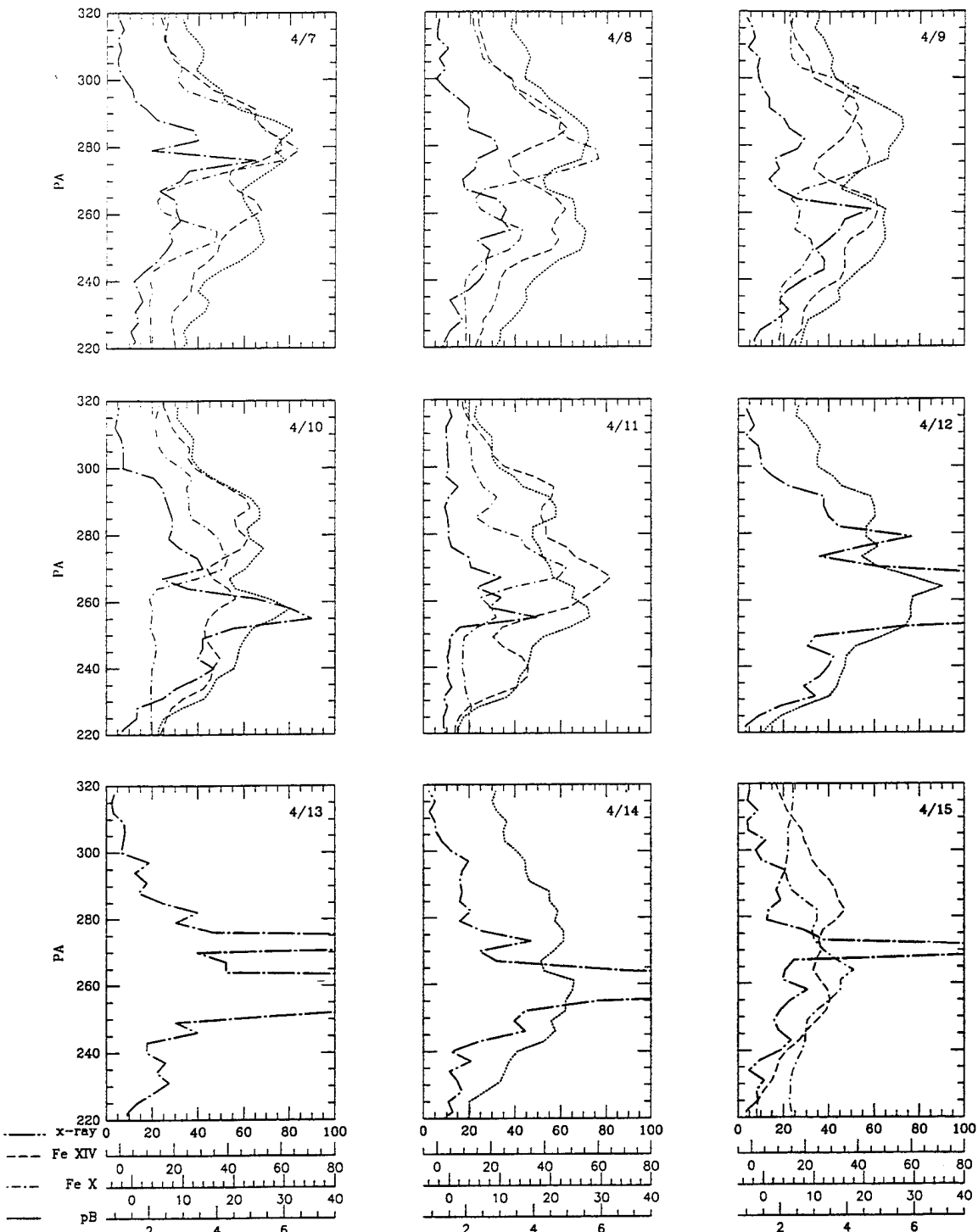


Figure 11: Contours of the left circular polarization of the 90 cm emission for 10-12 April 1993, superposed on the X-ray emission (top panels), and the corresponding magnetograms (bottom panels), where black refers to negative polarity, and white to positive. On each day the data were split into two halves. Subscripts  $a$  and  $b$  refer to sources imaged in the first and second half of the total observing time. Sources  $L_{a,b}$  corresponds to pointing at N0W35 on April 12, and  $L_{a',b'}$  to pointing at N0W0. (From Habbal et al. 1996)

West Limb  
7 - 15 April 1993 1.15 R<sub>s</sub>



18

Figure 12: Profiles of the Fe X 637.4 nm (dash-dot), Fe XIV 530.3 nm (long dash), X-ray (thick dash-dot), at 1.15 R<sub>s</sub>, and polarization brightness intensities (dot) at 1.16 R<sub>s</sub>, as a function of position angle along the west limb for 7-15 April 1993. A few data gaps existed in the ground-based observations. Fe X and Fe XIV are given in  $\text{erg cm}^{-2} \text{s}^{-1} \text{sr}^{-1}$ ; X-rays are in arbitrary units; and pB in  $10^{-7} \text{ B}/B_s$ , where  $B_s$  is the brightness of the solar disk. [From Habbal et al. 1996]

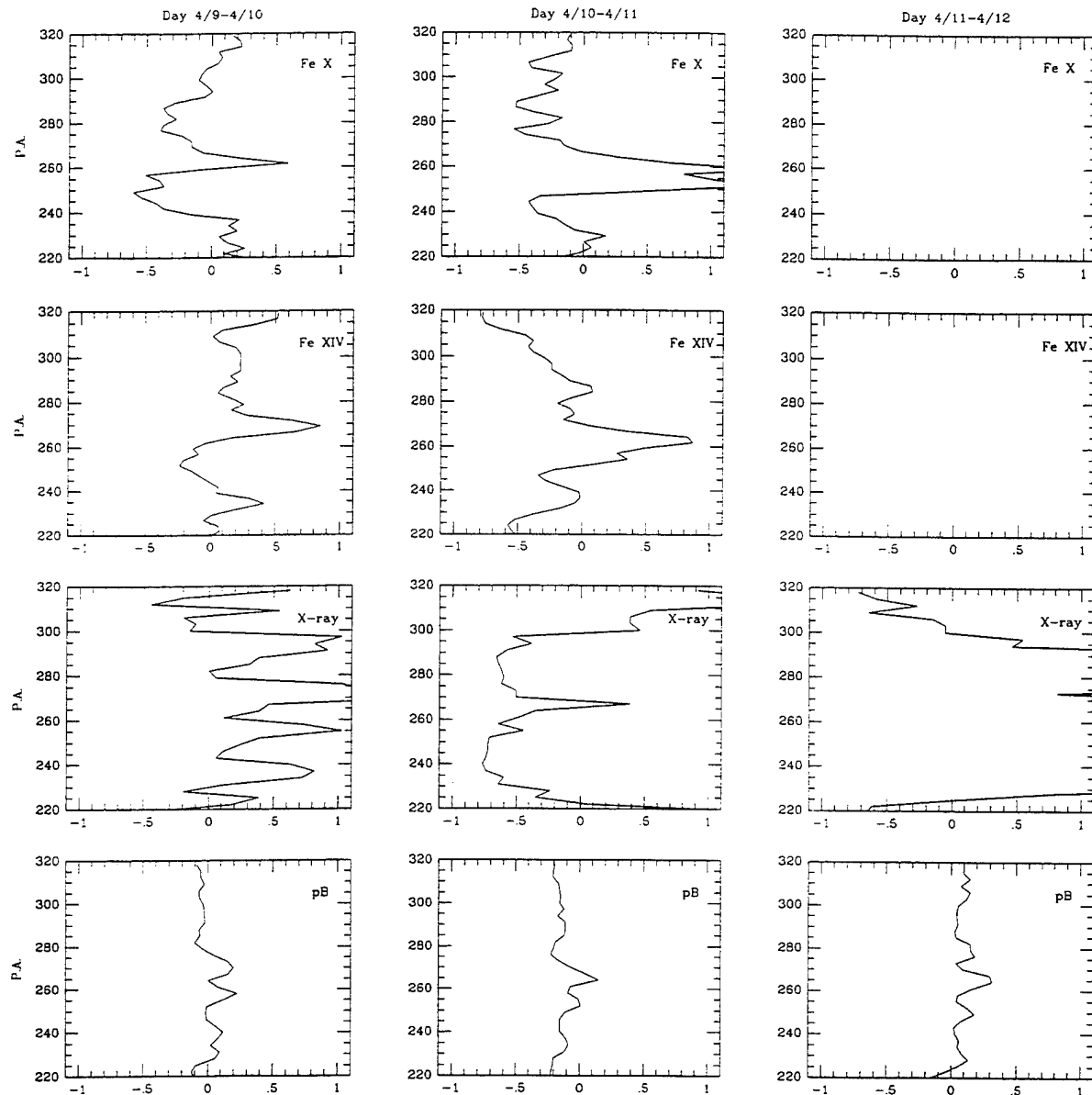


Figure 13: Relative change between three pairs of consecutive days, derived from the data in Figure 12. (From Habbal et al., 1996)

that the storm actually initiates the event.

### 3. CONCLUSION

The main results from the studies described in this report lead us to the following conclusions:

Temperature inferences in different coronal structures rely on the spectral lines used. Their judicious choice is particularly crucial for reliable inferences in coronal holes.

Limits on the helium abundance in the inner corona can be inferred from knowledge of the temperature and density, and their gradients in that region.

There exists a characteristic spatial separation of  $10''$ - $15''$  between the substructures within coronal holes, that is independent of the temperature of the emitting plasma, or the large scale overlying magnetic field.

Different temperature plasmas coexist at coronal heights regardless of the overlying large scale structure, such as active regions, quiet regions or coronal holes, and within these structures.

The spatial distribution of the temporal variability of the coronal emission has a very distinct temperature dependence, with a peak at  $10^5$  K, and is independent of the structure of the overlying large scale magnetic field.

In regard to some of the most spectacular forms of dynamic magnetic events, namely corona mass ejections, nonthermal emission as manifested in the form of type I noise storms observed at 90 cm, can serve as predictors for the occurrence of these events.

#### 4. REFERENCES

- Acton, L., et al 1992, *Science*, **258**, 618
- Arndt, M. B., Habbal, S. R. and Karovska, M. 1994, *Solar Phys.*, **150**, 165
- Ayers, G. R. and Dainty, J. C. 1988, *Opt. Lett.*, **13**, 547.
- Bohlin J. D., et al 1975, *Ap. J.*, **197**, L133
- Bürgi, A. 1992, *J. Geophys. Res.*, **97**, 3137
- Bürgi, A. and Geiss, J. 1986, *Solar Phys.*, **103**, 347
- Dere, K. P., et al 1989, *Solar Phys.*, **229**, 55
- Geiss, J., Hirt, P., and Leutwyler, H. 1970, *Solar Phys.*, **12**, 458
- Habbal, S.R. 1992, *Ann. Geophysicae*, **10**, 34
- Habbal, S.R. and Esser, R. 1994, *Ap. J.*, **421**, L59
- Habbal, S.R. and Grace, E. 1991, *Ap. J.*, **382**, 667
- Habbal, S. R. and Gonzalez, R. 1991, *Ap. J.*, **376**, L25
- Habbal, S. R., Esser, R., and Arndt, M. B. 1993, *Ap. J.*, **413**, 435.
- Habbal, S. R., Arndt, M. and Karovska, M. 1994, in *Solar Active Region Evolution: Comparing Models with Observations*, A.S.P. Conference Series, **68**, Edited by K. S. Balasubramaniam and G. W. Simon, 314.
- Habbal, S. R., Mossman, A., Gonzalez, R. and Esser, R., 1996, *J. Geophys. Res.*, in press.
- Karovska, M. and Habbal, S. H. 1991, *Ap. J.*, **371**, 402.
- Karovska, M. and Habbal, S. H. 1994, *Ap. J.*, submitted
- Karovska, M., Blundell, S. F. and Habbal, S. R. 1994, *Ap. J.*, **428**
- Koutchmy, S. 1977, *Solar Phys.*, **51**, 399
- Koutchmy, O., Koutchmy, S., Nitschelm, C., Sykora, J. and Smartt, R.N. 1988, in *Proceedings of the IXth NSO/SP Summer Symposium*, R.C. Altrock, (ed.), p. 256
- Leer, E., Holzer, T. E. and Shoub, E. C. 1992, *J. Geophys. Res.*, **97**, 8183
- Maartens, P., Acton, L., and Lemen, J. 1994, preprint
- Mullan, D. J., and Ahmad, I. A. 1982, *Solar Phys.*, **75**, 347
- Nisenson, P., Standley, C., and Hughes, J. 1989, *Bull. Am. Astron. Soc.*
- Parker, E. N. 1988, *Ap. J.*, **330**, 474
- Reeves, E.M., Huber, M.C.E. and Timothy, J.G. 1977a, *Appl. Opt.*, **16**, 837
- Reeves, E.M., Timothy, J.G., Huber, M.C.E. and Withbroe, G.L. 1977b, *Appl. Opt.*, **16**, 849
- Raymond, J. C. 1988, in *Radiation from Hot, Thin Plasmas*, ed. R. Pallavicini, (Dordrecht: Kluwer), 3
- Smartt, R.N. 1982, *Proc. SPIE*, **331**, 442
- Thieme, K. M., Schwenn, R. and Marsch, E. 1989, *Adv. Space Res.*, **9**, 127
- Tsuneta, S., et al 1991, *Solar Phys.*, **136**, 37
- Wang, Y.-M. 1993, *Ap. J.*, **410**, L123
- Wang, Y.-M. and Sheeley, N. R. Jr. 1991, *Ap. J.*, **372**, L45
- Withbroe, G. L., et al 1976, *Ap. J.*, **203**, 528

## 5. LIST OF PUBLICATIONS

### *5.1 PUBLICATIONS IN REFEREED JOURNALS*

- 1992 S. R. Habbal, "Coronal energy distribution and X-ray activity in the small scale magnetic field of the quiet Sun", *Annales Geophysicae*, **10**, 34.
- 1993 S. R. Habbal, R. Esser and M. B. Arndt, "How reliable are coronal hole temperatures deduced from observations", *Ap. J.*, **413**, 435-444.
- 1994 S. R. Habbal and R. Esser, "On the derivation of empirical limits on the Helium abundance in coronal holes below  $1.5 R_s$ ", *Ap. J.*, **421**, L59-L62.
- 1994 M. A. Arndt, S. R. Habbal and M. Karovska, "The discrete and localized nature of the variable emission from active regions", *Solar Phys.*, **150**, 165-178.
- 1994 M. Karovska, S. F. Blundell and S. R. Habbal, "Exploring the fine structure at the limb in a coronal hole", *Ap J.*, **428**, 854-859.
- 1994 M. Karovska and S. R. Habbal, "Dynamical structures of EUV macrospicules", *Ap J.*, **431**, L59-L62.
- 1994 S. R. Habbal, "Small scale structures in the solar corona", *Space Sci. Rev.*, **70**, 37-46.
- 1995 R. Esser, N. S. Brickhouse, S. R. Habbal, R. C. Altrock and H. C. Hudson, "Using Fe X 6374 Å and Fe XIV 5303 Å spectral line intensities to study the effect of the line of sight on coronal temperature inferences," *J. Geophys. Res.*, **100**, 19829-19838.
- 1995 S. R. Habbal, A. Mossman, R. Gonzalez, and R. Esser, "Radio, visible, and X-ray emission preceding and following a coronal mass ejection", submitted to *J. Geophys. Res.*.

### *5.2 PUBLICATIONS IN CONFERENCE PROCEEDINGS*

- 1994 S. R. Habbal, "Characteristic signatures of solar activity from the small scale magnetic field" in *Cool Stars, Stellar Systems, and the Sun*, Astronomical Society of the Pacific Conference Series, **64**, J.-P. Caillault (Ed.), 309-318.
- 1994 M. Karovska and M. Arndt, "The Fine Structure of the Solar Limb in a Coronal Hole," in *Proceedings of Kofu Symposium*, Sh. Enome and T. Hirayama (Eds.), Nobeyama Radio Observatory Report No. 360., p. 327.
- 1994 M. Karovska and H. C. Hudson, "Determining Point Spread Response Functions from Space Using Blind Iterative Deconvolution Algorithm, " "The Fine Structure of the Solar Limb in a Coronal Hole," in *Proceedings of Kofu Symposium*, Sh. Enome and T. Hirayama (Eds.), Nobeyama Radio Observatory Report No. 360., p. 330.
- 1994 S. R. Habbal, M. A. Arndt, and M. Karovska, "The discrete nature of the variable emission in active region loops", to appear in the Proceedings of the XIV NSO/SP Workshop on Solar Active Region Evolution - Comparing Models with Observations.
- 1994 R. Esser and S. R. Habbal, "Coronal holes and the solar wind", to appear in the Proceedings

of Cosmic Winds and the Heliosphere Workshop, held in Tucson, Arizona, October 1993.

1994 S. R. Habbal and R. Esser, "On the derivation of empirical limits on the Helium abundance in coronal holes below 1.5 Rs," to appear in Proceedings of the 28th ESLAB Symposium on the High Latitude Heliosphere.

1994 M. Karovska, S. R. Habbal, L. Golub, E. DeLuca, and H. C. Hudson, "Recovering the Fine Structures in Solar Images," to appear in the Proceedings of the 3rd SOHO Workshop: Solar Dynamic Phenomena and Solar Wind Consequences.

### *5.3 PAPERS PRESENTED AT CONFERENCES*

1992 S. R. Habbal and R. Esser, "Temperatures and Densities in the Inner Corona", 180th AAS Meeting, Columbus, OH.

1992 M. B. Arndt, A. Mossman and S. R. Habbal, "Temperature and Spatial Dependence of the Variable Emission from Active Regions", Gordon Research Conference, Plymouth, NH.

1993 M. Karovska, S. R. Habbal and F. Blundell, "Fine Structure at the Limb in a Coronal Hole", 181st AAS Meeting, Phoenix, AZ.

1993 M. Karovska, "Exploring the Dynamical Structure at the Limb in, a Coronal Hole", 24th Solar Physics Division Meeting, Palo Alto, CA.

1994 S. R. Habbal, A. Mossman, M. Karovska, R. Gonzalez and H. Hudson, "Coordinated cm and x-ray observations of an active region streamer", AGU meeting, Baltimore, MD.

1994 M. Karovska and H. C. Hudson, "Image Reconstruction and Enhancement of Yohkoh X-ray Observations of the Sun", AGU Meeting, Baltimore, MD.

1995 S. R. Habbal, N. S. Brickhouse, and R. Esser, "Exploring the temperature structure of coronal holes with a novel combination of visible Fe lines", Solar Wind 8 Conference, June.

1995 R. Esser, N. S. Brickhouse, and S. R. Habbal, Demonstrating the limitations of line ratio temperature diagnostic using Fe X and Fe XIV spectral line intensity observations, Solar Wind 8 Conference, June.

### *5.4 INVITED TALKS by S. R. Habbal*

1992 "Activity in the Quiet Sun", Physics Colloquium, Rensselaer Polytechnic Institute, April.

1992 "Observational Characteristics of Solar Activity in Small-Scale Magnetic Structures", Gordon Research Conference, Plymouth, New Hampshire, July.

1992 "The Small Scale Magnetic Field of the Sun and its Connection to Coronal Heating", Physics Colloquium, U. Mass, Dartmouth, November.

1993 "Observational Characteristics of Coronal Heating Mechanisms", University of Cincinnati Physics Colloquium, January.

- 1993 "Unraveling some of the Puzzles of Coronal Heating", Harvard-Smithsonian Center for Astrophysics Colloquium, March.
- 1993 "Small Scale Structures in the Solar Corona", Second SOHO Workshop, Elba, Italy, September.
- 1993 "Characteristic Signatures of Solar Activity from the Small Scale Magnetic Field", The 8th Cambridge Workshop on Cool Stars, Stellar Winds and the Sun, Athens, Georgia, October.
- 1993 "Temperature Structure, Spatial Structure and Variability of Emission from the Solar Corona", Monthly Meeting of the Amateur Telescope Makers of Boston, Cambridge, Massachusetts, November.
- 1993 "The Different Manifestations of Solar Activity", Physics Colloquium, University of New Hampshire, Durham, New Hampshire, November.
- 1994 "Plasma Parameters inferred from Coordinated Observations", IACG Workshop, Easton, MD, January.
- 1994 "Coordinated Ground-Based Observations", First Spartan Workshop, Goddard Space Flight Center, MD, March.
- 1994 "Modeling Efforts in the Solar Corona", First Spartan Workshop, Goddard Space Flight Center, MD, March.
- 1994 "Coordinated Ground and Space-Based Observations, and the Modeling of the Solar Wind," AGU Fall Meeting, San Francisco, December.
- 1995 "Probing the Acceleration Regions of the Solar Wind: Observational Techniques and Models", Colloquium at the High Altitude Observatory, Boulder, March.
- 1995 "Inferences if Coronal Hole Plasma Parameters from Observations", IAU Colloquium 154, Pune, India, January.

## REPORT DOCUMENTATION PAGE

Form Approved  
OMB No. 0704-0188

Public reporting burden for this collection of information is estimated to average 1 hour per response, including the time for reviewing instructions, searching existing data sources, gathering and maintaining the data needed, and completing and reviewing the collection of information. Send comments regarding this burden estimate or any other aspect of this collection of information, including suggestions for reducing this burden, to Washington Headquarters Services, Directorate for Information Operations and Reports, 1215 Jefferson Davis Highway, Suite 1204, Arlington, VA 22202-4302, and to the Office of Management and Budget, Paperwork Reduction Project (0704-0188), Washington, DC 20503.

1. AGENCY USE ONLY (Leave blank)	2. REPORT DATE	3. REPORT TYPE AND DATES COVERED
	2/6/96	Final Report - 7/1/91 - 7/31/95
4. TITLE AND SUBTITLE <b>HIGH RESOLUTION STUDIES OF THE STRUCTURE OF THE SOLAR ATMOSPHERE</b>		5. FUNDING NUMBERS G AFOSR-91-0244
6. AUTHOR(S) Dr. Shadia R. Habbal		
7. PERFORMING ORGANIZATION NAME(S) AND ADDRESS(ES) Smithsonian Institution Astrophysical Observatory 60 Garden Street Cambridge, MA 02138		8. PERFORMING ORGANIZATION REPORT NUMBER 16684340-P12S
9. SPONSORING/MONITORING AGENCY NAME(S) AND ADDRESS(ES) United States Air Force Air Force Office of Scientific Research Building 410 Bolling AFB, D.C. 20332-6448		10. SPONSORING/MONITORING AGENCY REPORT NUMBER 2311/AS
11. SUPPLEMENTARY NOTES		
12a. DISTRIBUTION / AVAILABILITY STATEMENT		12b. DISTRIBUTION CODE
13. ABSTRACT (Maximum 200 words)		
<p>Our approach has focused on exploring the physical characteristics of the coronal heating mechanisms, as manifested in coronal holes, quiet regions and active regions, using different data sets, data analysis techniques and image processing tools. The main results from these studies can be summarized as follows:</p> <p>(1) Temperature inferences in different coronal structures rely on the spectral lines used. Their judicious choice is particularly crucial for reliable inferences in coronal holes. (2) Limits on the helium abundance in the inner corona can be inferred from knowledge of the temperature and density, and their gradients in that region. (3) There exists a characteristic spatial separation of 10"-15" between the substructures within coronal holes, that is independent of the temperature of the emitting plasma, or the large scale overlying magnetic field. (4) Different temperature plasmas coexist at coronal heights regardless of the overlying large scale structure, such as active regions, quiet regions or coronal holes, and within these structures. (5) The spatial distribution of the temporal variability of the coronal emission has a very distinct temperature dependence, with a peak at 10<sup>5</sup> K, and is independent of the structure of the overlying large scale magnetic field. (6) In regard to some of the most spectacular forms of dynamic magnetic events, namely corona mass ejections, nonthermal emission as manifested in the form of type I noise storms observed at 90 cm, can serve as predictors for the occurrence of these events.</p>		
14. SUBJECT TERMS image processing, EUV solar data, variable emission		15. NUMBER OF PAGES 25
		16. PRICE CODE
17. SECURITY CLASSIFICATION OF REPORT unclassified	18. SECURITY CLASSIFICATION OF THIS PAGE unclassified	19. SECURITY CLASSIFICATION OF ABSTRACT unclassified
20. LIMITATION OF ABSTRACT		